Chapter 13

Lateral heterogeneity and the geoid: the importance of the surface kinematic constraints

A.M. Forte and W.R. Peltier

We apply the Green function technique to describe the internal load induced deformation of 3-D, self-gravitating, spherical shells of incompressible Newtonian fluid consisting either of a single constant-viscosity shell or of two adjacent shells of different viscosity. Using this method we derive closed form, analytic expressions for the kernel functions connecting the internal lateral heterogeneity of density to the horizontal divergence of the surface flow and to the non-hydrostatic geoid. Although the geoid constrains only the ratio of the upper and lower mantle viscosities, the horizontal divergence field constrains their absolute values. We find that both surface divergence and geoid fields are best fit with only a factor of eight viscosity increase at 1200 km depth. We point out, however, that the coupling of poloidal and toroidal flow in the Earth's mantle, which is required to understand surface velocity spectra, will most probably allow us to reduce the viscosity increase required by the geoid data.

1. Introduction

Current inferences of the spherically symmetric viscosity distribution in the Earth's mantle rely upon internal loading schemes which relate the seismically inferred lateral density variations in the Earth to the large-scale undulations of the non-hydrostatic geoid (e.g., Hager, 1984). These internal loading calculations all seem to require an increase in the viscosity at the 670 km seismic discontinuity which is considerably greater than the viscosity increase required by glacial isostatic adjustment analyses (e.g., Peltier, 1982). In

N.J. Vlaar, G. Nolet, M.J.R. Wortel & S.A.P.L. Cloetingh (eds), Mathematical Geophysics, 291-323.

this report we will present an alternative formulation of the internal loading problem and we will later argue that a likely reason for the discrepancy between the viscosity inferences obtained from post-glacial rebound data and isostatic geoid anomalies is that the Newtonian viscous flow models used in current internal loading analyses are unable to satisfy the surface kinematic constraints provided by the observed tectonic plate velocities.

The mathematical method most commonly used to relate geophysical surface observables, such as the geoid, to lateral density variations in the mantle is the propagator matrix technique (e.g., Richards and Hager, 1984; Ricard et al., 1984). In this report we will show that the Green function technique employed by Parsons and Daly (1983) is a mathematically straightforward alternative to the propagator matrix schemes allowing one to readily derive analytic, closed-form, expressions for the kernels which connect lateral density heterogeneity at depth to the surface observables. The Green functions considered by Parsons and Daly (1983) were derived for a 2-D cartesian geometry where the effects of self-gravitation were ignored; here we will show how the Green function method may be extended to 3-D, spherical, self-gravitating shells of constant viscosity and also to the case of shells consisting of two layers having different viscosities. The Green function method will be employed to derive expressions for the kernel functions describing the non-hydrostatic geoid and the horizontal divergence of the convective flow field produced at the Earth's surface by lateral density variations in the mantle.

Previous attempts to model the non-hydrostatic geoid (e.g., Hager, 1984) have ignored the importance of the observed surface plate kinematics and the constraints they provide on the viscosity structure of the mantle. The equipartition of kinetic energy between the poloidal and toroidal components of the observed surface-plate velocity field is likely to have a direct bearing on our ability to properly model the geoid. Despite the complications produced by the poloidal-toroidal coupling of the convective flow in the mantle we will demonstrate, using the simple physical models that will be presented, that on the whole the observed large-scale plate motions are those expected to exist on the basis of the seismic tomographic inferences of the internal density heterogeneity. This last result provides strong and convincing support for the hypothesis that the large-scale tectonic plate motions are the surface expression of deep-seated convection in the Earth's mantle.

In section 2 of the report we will briefly summarize the main features of the observed tectonic plate velocities. In section 3 we present our extension of the Green function method which is then employed to infer the contrast between the viscosities of the upper and lower mantles. In section 4, we discuss the trade-off we believe to exist between the conversion of poloidal to toroidal flow and the strength of the viscosity contrast required by the observed non-hydrostatic geoid. Finally, in section 5 of this report, we provide our main conclusions.

2. Present-day tectonic plate velocities

Employing the Wilson-Morgan hypothesis of fixed hot spots, Minster and Jordan (1978) have obtained a model for the absolute, present-day, tectonic plate velocities which are depicted in Fig. 1. We shall refer to this velocity field as the "observed surface-plate velocities". From the observed surface-plate velocities we have calculated the spherical harmonic coefficients of two scalars, the horizontal divergence and the radial vorticity, which completely characterize the tectonic plate motions:

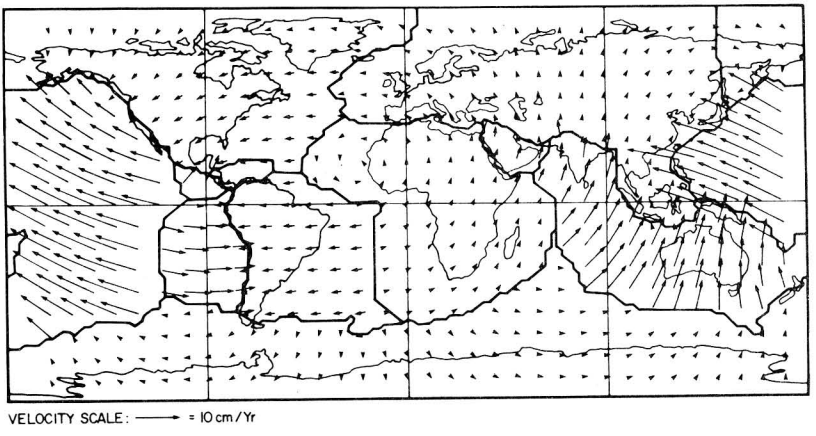

Figure 1. Surface plate velocity field constructed from the absolute angular velocity vectors of Minster and Jordan (1978) in the "hot spot" frame.

$$\nabla_H \cdot \mathbf{v} = \sum_{l,m} D_l^m \, Y_l^m(\theta,\phi) \tag{1a}$$

$$\hat{\mathbf{r}} \cdot (\nabla \times \mathbf{v}) = \sum_{l,m} V_l^m \, Y_l^m(\theta,\phi) \, . \tag{1b}$$

In equation (1) $\mathbf{v}$ is the observed surface-plate velocity field and D_l^m and V_l^m are, respectively, the harmonic coefficients of the horizontal divergence and radial vorticity.

An alternative scalar representation of the surface kinematics, previously employed by Hager and O'Connell (1978), is obtained by describing the observed surface-plate velocities in terms of poloidal and toroidal components:

$$\mathbf{v} = \sum_{l,m} S_l^m \, \hat{\mathbf{r}} \times \mathbf{\Lambda} \, Y_l^m(\theta,\phi) + \sum_{l,m} T_l^m \, \mathbf{\Lambda} \, Y_l^m(\theta,\phi) \, . \tag{2}$$

In equation (2) we have employed the angular momentum operator $\mathbf{\Lambda} = \mathbf{r} \times \nabla$ (Backus, 1958) and S_l^m and T_l^m are, respectively, the poloidal and toroidal scalars. A description of the surface kinematics in terms of the two scalars appearing in (1) is completely equivalent to a description in terms of the scalars appearing in (2) since one may readily show that

$$S_l^m = \frac{a D_l^m}{l(l+1)} \tag{3a}$$

$$T_l^m = \frac{-a V_l^m}{l(l+1)} \, , \tag{3b}$$

where a is the radius of the Earth.

The harmonic coefficients D_l^m and V_l^m (tabulated in Forte and Peltier, 1986) have been used to synthesize the maps of horizontal divergence and radial vorticity presented in Fig. 2. From this figure it is evident that the horizontal divergence scalar is necessary to represent two of the types of plate boundary which are observed in nature: the ridges and

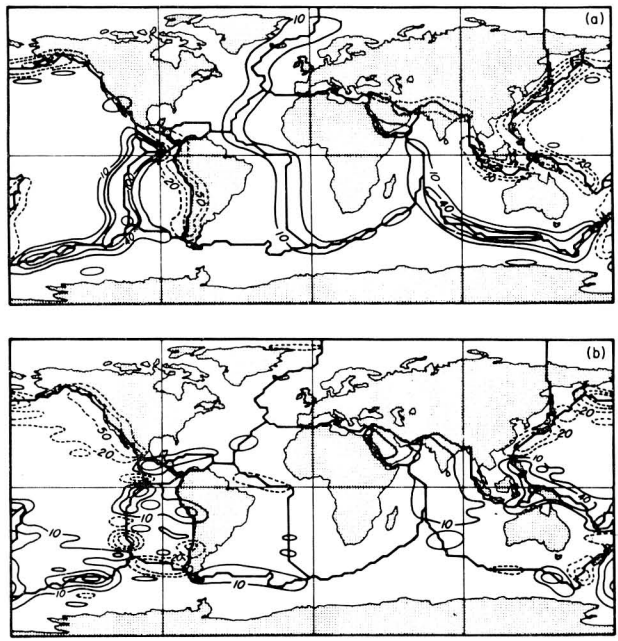

Figure 2. (a) Surface divergence up to degree and order 32. The contour interval is 30 x 10^{-9} rad/yr. and the individual contour levels are in units of 10^{-9} rad/yr. The dashed contour lines indicate negative divergence. (b) Radial vorticity to degree and order 32. The contour interval and units are as in (a). The dashed contour lines indicate negative vorticity (i.e., clockwise circulation).

trenches. The radial vorticity scalar is necessary to represent the third type of plate boundary: the transform fault.

The partitioning of kinetic energy between the poloidal and toroidal components of the observed surface-plate velocities may be determined by calculating their degree variances, σ_l:

$$\sigma_l \text{ (poloidal)} = \left[\sum_{m=-l}^{l} S_l^m S_l^{m*} \right]^{1/2} \tag{4a}$$

$$\sigma_l \text{ (toroidal)} = \left[\sum_{m=-l}^{l} T_l^m T_l^{m*} \right]^{1/2}, \tag{4b}$$

where the asterisk denotes complex conjugation. These degree variances are shown in Fig. 3(a) where one observes that there is an almost exact equipartition of kinetic energy between the poloidal and toroidal components; this result was first obtained by Hager and O'Connell (1978) who did not further consider its importance except in the context of their Stokes flow extrapolation to depth of the observed surface-plate velocities. In a spherical shell of chemically uniform fluid with physical properties that vary with radius only one

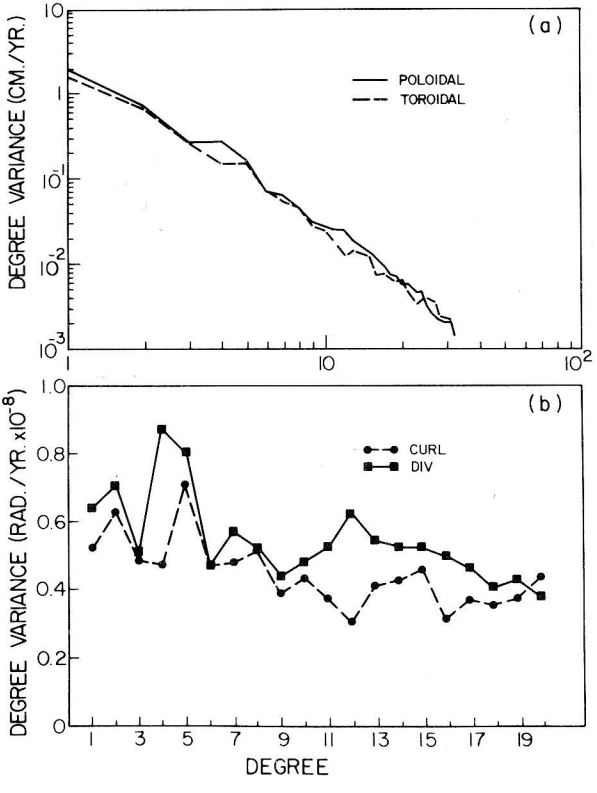

Figure 3. (a) Degree variance of the poloidal and toroidal components of the surface velocity field. (b) Degree variance of the horizontal divergence and radial vorticity fields derived from the surface plate velocities.

expects thermally induced buoyancy forces to produce poloidal flow only. The factors that are most probably responsible for generating the required large flux of energy from poloidal to toroidal flow are the extreme lateral variations of viscosity in the mantle (e.g. Hager and O'Connell, 1978) as well as the presence of chemically differentiated, continental crust which is buoyant and therefore cannot be subducted (Peltier, 1985). In Fig. 3(b) we show the degree variances of the horizontal divergence and radial vorticity scalars and it will be noted in particular that the divergence spectrum is characterized by a well-defined peak at $l = 4, 5$.

3. Predicting surface motions and the geoid from seismically inferred mantle heterogeneity

3.1 Green function for a constant-viscosity mantle

The Boussinesq hydrodynamic equations which we consider describe the conservation of mass and momentum in a viscous fluid:

$$\nabla \cdot \mathbf{u} = 0 , \tag{5}$$

$$\rho_o \mathbf{g}_1 + \rho_1 \mathbf{g}_o - \nabla P_1 + \eta \, \Delta \mathbf{u} = 0 . \tag{6}$$

The quantities with subscript 1 are perturbations to the hydrostatic reference state which is denoted by the subscript o. The inertial force terms have been ignored in equation (6) since the Earth's mantle is characterized by an essentially infinite Prandtl number. We will adopt the sign convection that the perturbed body force $\mathbf{g}_1$ appearing in the self-gravitation term $\rho_o \mathbf{g}_1$ in (6) is given by

$$\mathbf{g}_1 = \nabla \phi_1 , \tag{7}$$

where ϕ_1, the perturbed gravitational potential, then satisfies

$$\Delta \phi_1 = -4\pi G \rho_1 . \tag{8}$$

The body force $\mathbf{g}_o$ is simply given by

$$\mathbf{g}_o = -\frac{g_o}{r} \mathbf{r} , \tag{9}$$

where g_o is the (approximately) constant gravitational acceleration in the Earth's mantle.

Equation (5) shows that $\mathbf{u}$ is solenoidal and may therefore be represented as

$$\mathbf{u} = \nabla \times \Lambda p + \Lambda q \tag{10}$$

where p and q are, respectively, the poloidal and toroidal scalars (Backus, 1958). Substitution of results (7), (9), and (10) into equation (6) and application of $\nabla\times$ to the resulting equation yields

$$\Lambda \frac{\rho_1 g_o}{r} + \eta \, \nabla \times \Lambda \, \Delta q - \eta \, \Lambda \, \Delta^2 p = 0 . \tag{11}$$

If one now applies the operator $\Lambda\cdot$ to equation (11) and uses the result $\Lambda\cdot(\nabla \times \Lambda) = 0$ (Backus, 1958) then the following is obtained:

$$\eta \, \Lambda^2 \Delta^2 p = \Lambda^2 \frac{\rho_1 g_o}{r} , \tag{12}$$

where the operator $\Lambda^2 = \Lambda\cdot\Lambda$ is characterized by the property

$$\Lambda^2 \, Y_l^m(\theta,\phi) = -\, l(l+1) \, Y_l^m(\theta,\phi) \tag{13}$$

and $Y_l^m(\theta,\phi)$ is the complex spherical harmonic function which is normalized such that

$$\frac{1}{4\pi} \int_S Y_l^m(\theta,\phi) \, Y_s^{t*}(\theta,\phi) \, dS = \delta_{ls} \, \delta_{mt} , \tag{14}$$

where S denotes integration over the surface area of the unit sphere. If one expands the quantities p and ρ_1, in (12), in terms of spherical harmonics and uses results (13) and (14) then the following important equation is obtained:

$$D_l^2\, p_l^m(r) = \frac{g_o}{\eta}\,\frac{(\rho_1)_l^m(r)}{r}\,, \tag{15}$$

where $p_l^m(r)$ and $(\rho_1)_l^m(r)$ are the radially-varying spherical harmonic coefficients of the scalars p and ρ_1 respectively. D_l^2 is the transformed biharmonic operator Δ^2 and D_l is defined as

$$D_l = \frac{d^2}{dr^2} + \frac{2}{r}\,\frac{d}{dr} - \frac{l(l+1)}{r^2}\,.$$

Now since $\mathbf{r}\cdot\boldsymbol{\Lambda} = 0$, it is evident from equation (11) that the toroidal scalar is governed by the following equation:

$$\eta\,\boldsymbol{\Lambda}^2\,\Delta q = 0\,,$$

and expanding q in terms of spherical harmonics this last result becomes:

$$D_l\, q_l^m(r) = 0\,. \tag{16}$$

Equations (15) and (16) show that when the dynamic viscosity, η, is assumed constant then lateral density variations will only excite a poloidal flow field; this is also true for the more general case in which the viscosity is an arbitrary function of radius as shown, for example, by Arkani-Hamed and Toksöz (1984).

The poloidal flow Green function, $p_l^m(r,r')$, is found by solving

$$D_l^2\, p_l^m(r,r') = \delta(r - r')\,, \tag{17}$$

where $\delta(r)$ is the Dirac delta function and r' is the radius at which the δ-function load is placed. The Green function will depend on the boundary conditions assumed at the Earth's surface ($r=a$) and at the core-mantle boundary (CMB; $r=b$). If one assumes that, on the whole, the tectonic plates are participating in the large scale flow in the mantle then a free-slip boundary condition at $r=a$ is suggested. We will also assume a free-slip condition at the CMB. The derivation of the poloidal flow Green function which satisfies these boundary conditions is presented in Appendix A. Once the Green function has been obtained it is clear from equations (15) and (17) that the poloidal scalar will be given by

$$p_l^m(r) = \frac{g_o}{\eta}\int_b^a \frac{(\rho_1)_l^m(r')}{r'}\, p_l^m(r,r')\, dr'\,. \tag{18}$$

The toroidal flow present in the observed surface plate velocities obviously poses a problem when attempting to predict the plate motions using the poloidal scalar of equation (18). We believe however that the conversion of poloidal to toroidal flow occurs largely near the Earth's surface where the lateral variations in rheology and chemistry are the most extreme. This suggests then that density heterogeneity below the lithosphere will mostly excite poloidal flow thus maintaining the validity of equation (15). We found moreover (Forte and Peltier, 1986) that a strong correlation exists between the horizontal divergence and the seismically inferred lateral heterogeneity in the upper mantle at degrees 2 and 4; this suggests that there is a linear relationship between these two fields and that it should therefore be possible to model the horizontal divergence at these two degrees with a spherically symmetric viscosity model.

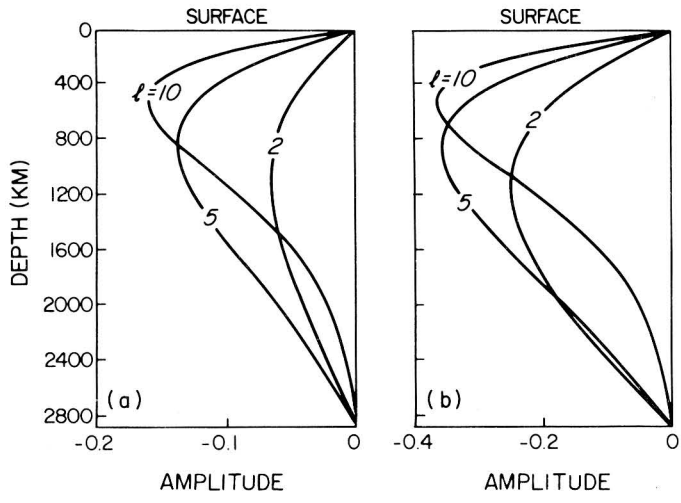

Figure 4. Kernels for an incompressible, homogeneous mantle with free-slip conditions at the surface and CMB.: (a) Horizontal divergence kernels (b) Geoid kernels for a self-gravitating mantle.

The kernel function, $S_l(r')$, which allows us to predict the spherical harmonic coefficients of the horizontal divergence at $r=a$ from the lateral density variations in a constant-viscosity mantle is derived in Appendix A where we show

$$(\nabla_H \cdot \mathbf{u})_l^m(r=a) = \frac{g_o}{\eta} \int_b^a S_l(r')\,(\rho_1)_l^m(r')\,dr' \,. \tag{19}$$

In Fig. 4(a) we show the function $S_l(r')$ for several degrees. The density perturbation, $(\rho_1)_l^m(r)$, is obtained from models M84C of Woodhouse and Dziewonski (1984) and L02.45 of Dziewonski (1984) where we are assuming that the lateral variations in seismic wave speeds are caused solely by lateral temperature variations:

$$(\rho_1)_l^m = \begin{cases} \dfrac{(\partial\rho/\partial T)}{2v_s(\partial v_s/\partial T)}\,[\delta(v_s^2)]_l^m\,, & 25\text{ km} \le z \le 670\text{ km} \\ \dfrac{(\partial\rho/\partial T)}{(\partial v_p/\partial T)}\,[\delta(v_p)]_l^m\,, & 670\text{ km} \le z \le 2895\text{ km} \end{cases} \tag{20}$$

The temperature derivatives we use in (20) were obtained by Anderson et al. (1968) from laboratory analyses of spinel. Forte and Peltier (1986) show that the temperature derivatives of spinel are probably reasonable estimates of the actual values. The degree correlations (e.g. O'Connell, 1971) between the observed horizontal divergence and the divergence predicted using (19) are shown in Table 1 where one observes that excellent correlations are obtained at $l=2$ and 4 as expected.

Table 1 Degree correlations between predicted surface divergence for a homogeneous mantle and observed surface divergence

Degree, l	Correlation Coefficient	Significance Level, α
$l=2$	.80	$90\% < \alpha < 95\%$
$l=3$	.30	$\alpha < 80\%$
$l=4$	.68	$95\% < \alpha < 98\%$
$l=5$	.28	$\alpha < 80\%$

The straightforward manner with which the kernel functions for the non-hydrostatic geoid are derived is a good illustration of the flexibility offered by the Green function method. The harmonic coefficients of the interior gravitational potential produced only by the internal density heterogeneity in the mantle are:

$$(U_{int})_l^m(r) = \frac{4\pi G}{2l+1} \int_b^a r'^2 \frac{r_<^l}{r_>^{l+1}} (\rho_1)_l^m(r')\, dr' , \tag{21}$$

where $b \leq r \leq a$, $r_< = \min(r, r')$, and $r_> = \max(r, r')$. The harmonic coefficients of the internal potential produced by the deflected surface boundary at $r=a$ are:

$$(U_a)_l^m(r) = \frac{4\pi G a}{2l+1} (\rho_o - \rho_w) \left[\frac{r}{a}\right]^l \delta a_l^m , \tag{22}$$

where δa_l^m are the harmonic coefficients of the deflection of the Earth's surface, $\delta a(\theta,\phi)$, from its reference position and we have assumed that the mantle of density ρ_o is overlain by ocean with density ρ_w. The expression for the internal potential produced by the deflected CMB is:

$$(U_b)_l^m(r) = \frac{4\pi G b}{2l+1} (\rho_c - \rho_o) \left[\frac{b}{r}\right]^{l+1} \delta b_l^m , \tag{23}$$

where ρ_c is the density of the outer core and δb_l^m are the harmonic coefficients describing the deflection of the CMB. We expect that the deflections of the phase-change boundaries in the mantle are likely to contribute significantly to the Earth's gravitational potential but in the absence of information regarding these deflections we will state that the total perturbed potential, ϕ_1, is simply given by:

$$(\phi_1)_l^m(r) = (U_{int})_l^m(r) + (U_a)_l^m(r) + (U_b)_l^m(r) . \tag{24}$$

The surface deflection $\delta a(\theta,\phi)$ may be determined from the condition that the σ_{rr} component of the stress tensor will be continuous at the bounding surface:

$$\delta a(\theta,\phi) = \frac{P_1(r=a)}{g_o(\rho_o-\rho_w)} - \frac{2\eta}{g_o(\rho_o-\rho_w)}\left[\frac{\partial u_r}{\partial r}\right]_{r=a}, \tag{25}$$

where P_1 is the non-hydrostatic pressure and $u_r = \hat{\mathbf{r}}\,\mathbf{u}$. The deformed CMB will also be described by (25) except that ρ_w is replaced by ρ_c and all quantities are evaluated at r=b. In Appendix A we provide complete details of the derivation of the self-gravitating geoid kernels, $G_l(r')$, which allow us to predict the geoid:

$$(Ge)_l^m = \frac{3}{(2l+1)\bar{\rho}} \int_b^a G_l(r')\,(\rho_1)_l^m(r')\,dr', \tag{26}$$

where $(Ge)_l^m$ are the harmonic coefficients of the predicted geoid and $\bar{\rho}$ is the average density of the Earth. The behaviour of the function $G_l(r')$ is shown in Fig. 4(b) where it is observed that the kernels all have a negative sign. The negative sign of these kernels is due to the dominant negative contribution of the flow-induced deflection of the surface boundary compared to the weaker positive contribution of the internal lateral density variations (e.g. Hager, 1984). A comparison of equations (19) and (26) shows that, in contrast to the predicted horizontal divergence field, the predicted non-hydrostatic geoid produced by lateral density variations in a constant-viscosity mantle will not depend on the viscosity.

In Table 2 we present the degree correlations between the observed, GEM10B, non-hydrostatic geoid of Lerch et al. (1979) (filtered by removal of the hydrostatic flattening determined by Nakiboglu (1982)) and the geoid predicted using (26). From an analysis of the degree correlations between the observed, non-hydrostatic geoid and the seismically inferred mantle heterogeneities we found (Forte and Peltier, 1986) that the kernels describing the degree-2 and 3 geoid should have maximum (negative) amplitudes in the lower mantle and negligible amplitude in the upper mantle while for $l \geq 4$ the kernels should generally have maximum (positive) amplitudes in the mid-mantle and negligible amplitudes elsewhere. An examination of the shapes of the geoid kernels shown in Fig. 4(b) will then reveal why the correlations in Table 2 are generally poor.

Table 2 Degree correlations between predicted geoid for a homogeneous mantle and observed non-hydrostatic geoid

Degree, l	Correlation Coefficient	Significance Level, α
l=2	-.01	$\alpha < 80\%$
l=3	.53	$\alpha < 80\%$
l=4	-.51	$80\% < \alpha < 90\%$
l=5	.60	$\alpha \approx 95\%$

3.2 Green function for a two-layer mantle

A simple Earth model that permits one to determine the effects of viscosity stratification is an incompressible mantle divided into two layers having different viscosities. We continue to assume that a whole-mantle convective flow exists and we do not therefore consider the case in which the depth of the viscosity jump also coincides with a chemical discontinuity which occurs if there is a layered convective circulation.

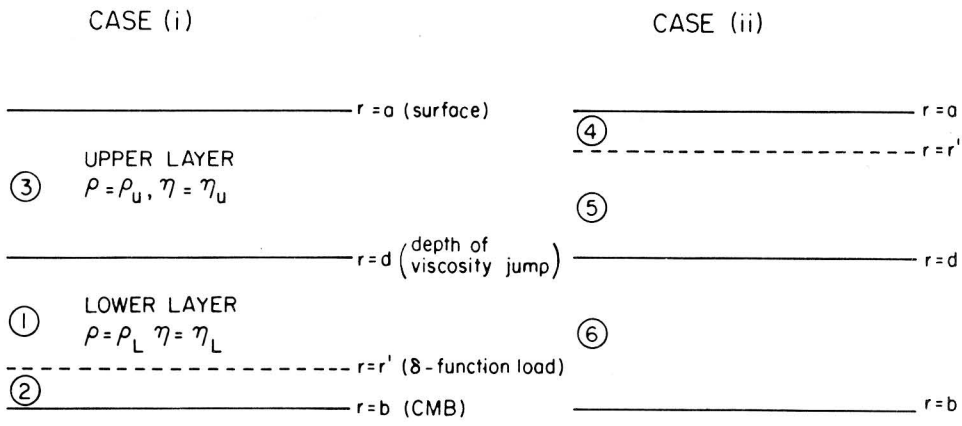

Figure 5. Schematic diagram of the geometry for the two-layer Green function.

The dynamic viscosity in each layer is assumed constant and thus equation (15) is valid in each layer. Since the delta-function loads may be placed in either layer the problem consists of treating two cases: case (i) - find the poloidal flow Green function for a δ-function load in the lower layer, and case (ii) - find the poloidal flow Green function for a δ-function load in the upper layer. The Green function for case (i) will thus satisfy the following equation:

$$D_l^2(p_L)_l^m(r,r') = \begin{cases} 0 & d < r < a \\ \delta(r-r') & b < r < d \end{cases}, \tag{27}$$

while the Green function for case (ii) satisfies:

$$D_l^2(p_u)_l^m(r,r') = \begin{cases} \delta(r-r') & d < r < a \\ 0 & b < r < d \end{cases}. \tag{28}$$

where $r=d$ is the radius at which the viscosity jump occurs. It is evident from equations (27) and (28) that the mantle will in each case consist of three regions which are shown and numbered for reference in Fig. 5. The poloidal flow Green function will again satisfy free-slip boundary conditions at the Earth's surface and at the CMB. From equations (15), (27), and (28) one may verify that the poloidal scalar is given by:

$$p_l^m(r) = \frac{g_o}{\eta_u} \int_d^a \frac{(\rho_1)_l^m(r')}{r'} (p_u)_l^m(r,r')\, dr'$$

$$+ \frac{g_o}{\eta_L} \int_b^d \frac{(\rho_1)_l^m(r')}{r'} (p_L)_l^m(r,r')\, dr' \,, \tag{29}$$

where η_u and η_L are, respectively, the viscosities of the upper and lower layers. If we let, for example, $(p_5)_l^m(r,r')$ denote the Green function $(p_u)_l^m(r,r')$ in the region $d < r < r'$ (i.e. layer 5 in Fig. 5) then the numbering scheme in Fig. 5 allows us to rewrite (29) as:

$$p_l^m(r) = \frac{g_o}{\eta_u} \int_r^a \frac{(\rho_1)_l^m(r')}{r'} (p_5)_l^m(r,r')\, dr'$$

$$+ \frac{g_o}{\eta_u} \int_d^r \frac{(\rho_1)_l^m(r')}{r'} (p_4)_l^m(r,r')\, dr' \tag{30a}$$

$$+ \frac{g_o}{\eta_L} \int_b^d \frac{(\rho_1)_l^m(r')}{r'} (p_3)_l^m(r,r')\, dr' \,, \text{ for } d < r < a$$

and

$$p_l^m(r) = \frac{g_o}{\eta_u} \int_d^a \frac{(\rho_1)_l^m(r')}{r'} (p_6)_l^m(r,r')dr'$$

$$+ \frac{g_o}{\eta_L} \int_r^d \frac{(\rho_1)_l^m(r')}{r'} (p_2)_l^m(r,r')\, dr' \tag{30b}$$

$$+ \frac{g_o}{\eta_L} \int_b^r \frac{(\rho_1)_l^m(r')}{r'} (p_1)_l^m(r,r')dr' \,, \text{ for } b < r < d$$

The complete details of the Green function derivation for the two-layer mantle will be found in Appendix B. In this Appendix we also derive analytic expressions for the kernel function, S_l, describing the horizontal divergence:

$$(\nabla_H \cdot \mathbf{u})_l^m(r=a) = \frac{g_o}{\eta_u} \int_b^a S_l(r';\eta_L/\eta_u,d)\, (\rho_1)_l^m(r')dr' \,. \tag{31}$$

From (31) it is evident that although S_l depends on the ratio of the viscosities the multiplicative factor, η_u, implies that the amplitude of the predicted horizontal divergence depends on the absolute value of the viscosity in each layer. In contrast, the predicted non-hydrostatic geoid will depend only on the ratio of the viscosities of the two layers:

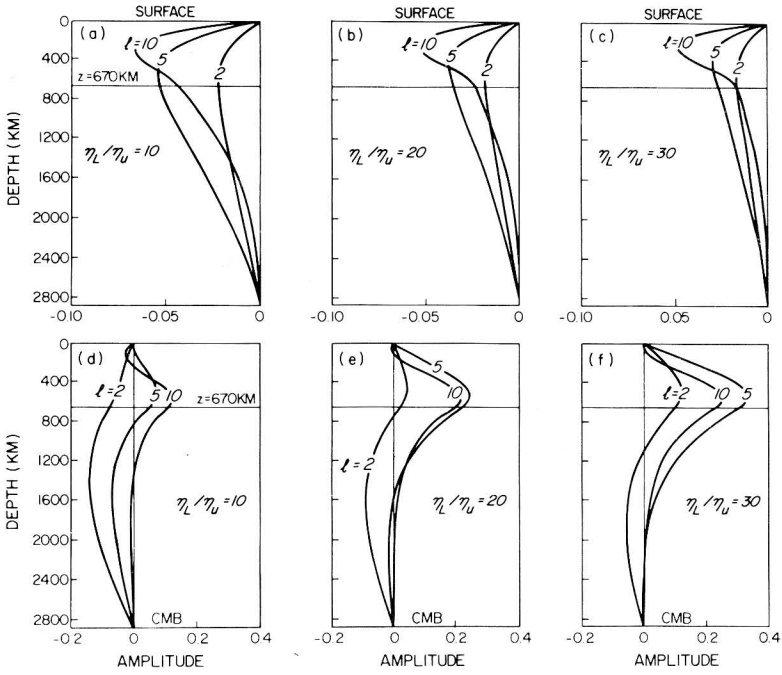

Figure 6. Kernels for an incompressible, two-layer mantle with free-slip conditions at the surface and CMB and viscosity jump at z=670 km. (a), (b), and (c) Horizontal divergence kernels; (d), (e) and (f) Geoid kernels for a self-gravitating mantle.

$$(Ge)_l^m = \frac{3}{(2l+1)\bar{\rho}} \int_b^a G_l(r';\eta_L/\eta_u,d)\,(\rho_1)_l^m(r')dr' \ , \tag{32}$$

where G_l is the geoid kernel, derived in Appendix B, for the self-gravitating, two-layer mantle.

The behaviour of the kernel functions describing the horizontal divergence and the geoid for the case d = 5701 km (i.e. depth z = 670 km) are shown in Fig. 6 for several viscosity ratios. A comparison of Figs. 4 and 6 shows that the effect of increasing the viscosity at depth has "split" the divergence and geoid kernels: the longest wavelength geoid (l = 2,3) is now more sensitive to lateral density variations in the lower mantle while the horizontal divergence is most sensitive to lateral density variations in the upper mantle. One also observes that the geoid kernels in Fig. 6 become increasingly positive as the viscosity of the lower layer increases since the mantle becomes "stiffer" thus diminishing the negative contribution to the geoid provided by the surface boundary deflection; this allows the positive contribution of the internal density anomalies to the geoid to become dominant (Hager, 1984). In Fig. 7 we show profiles of the divergence and geoid kernels for the case d = 5171 km (z = 1200 km). The kernel functions shown in Figs. 6 and 7 show that the predicted geoid will be very sensitive to changes in both the viscosity ratio and the

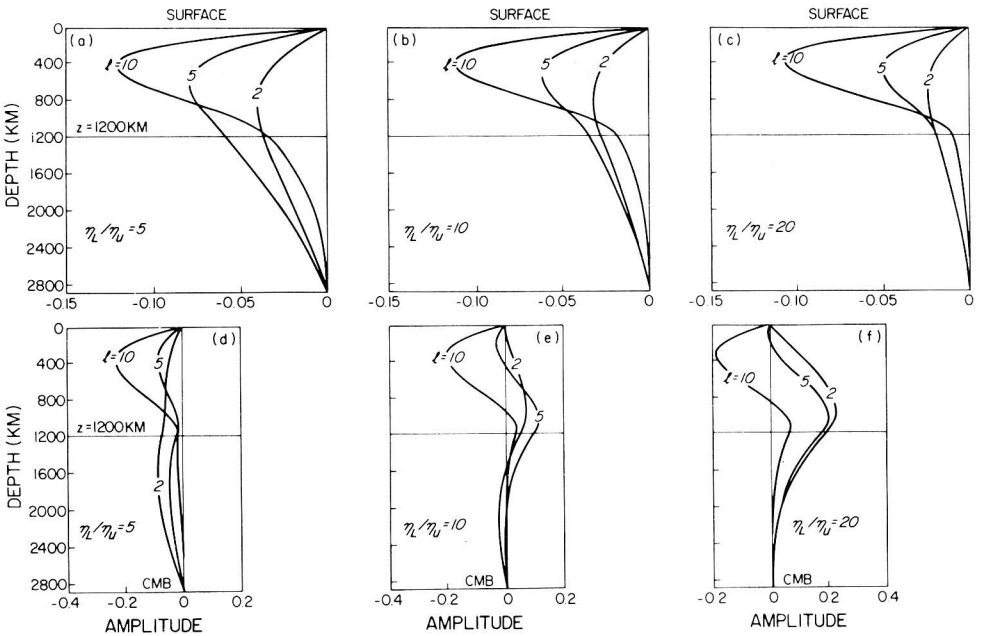

Figure 7. Kernels for an incompressible, two-layer mantle with free-slip conditions at the surface and CMB and viscosity jump at z=1200 km.: (a), (b) and (c) Horizontal divergence kernels; (d), (e) and (f) Geoid kernels for a self-gravitating mantle.

depth of the viscosity jump while the predicted horizontal divergence will be relatively insensitive to these changes.

The degree correlations of the geoid predicted using (32) and the observed non-hydrostatic geoid are presented in Fig. 8. When the boundary depth is at z = 670 km the best correlations for degrees 2 and 3 occur when $16 < \eta_L/\eta_u < 18$ but the correlation at l = 4 is very poor in this range while the correlation for l = 5 has the "wrong" sign. The best fit, at all degrees, is obtained when z = 1200 km since for $\eta_L/\eta_u = 8$ the correlations for l = 2-5 are all positive and those at l = 2,3 and 5 are more than 90% significant. In Fig. 9 we show the degree variances of the predicted geoid.

We noted previously that the profiles of the horizontal divergence kernels are relatively insensitive to changes in the viscosity ratio and the depth of the viscosity jump. The degree correlations of the horizontal divergence predicted using (31) and the observed divergence are therefore expected to be fairly constant and this is confirmed in Fig. 10. The most appropriate viscosity ratio, η_L/η_u, and radius of the boundary, d, must then be determined by fitting the predicted geoid to the observed non-hydrostatic geoid. An objective measure of fit which includes the information provided by both the degree correlations and the degree variances is the root mean square (rms) error, δ_{rms}, defined by:

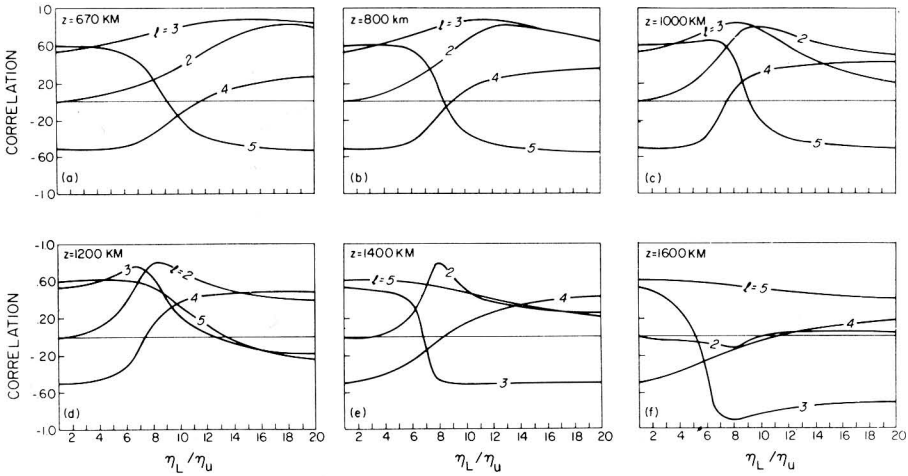

Figure 8. Degree correlations of corrected, non-hydrostatic, geoid (Nakiboglu, 1982) obtained from the GEM10B geopotential model (Lerch et al., 1979) with the predicted geoid, as a function of viscosity contrast and depth of viscosity jump.

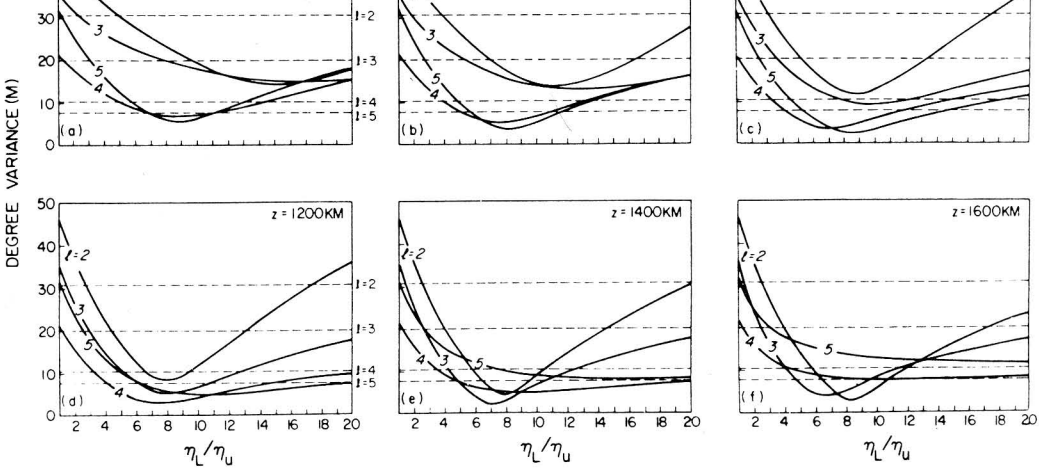

Figure 9. Degree variances (in metres) of the predicted geoid, for a two-layer mantle, as a function of viscosity contrast and depth of viscosity jump. The dashed horizontal lines are the degree variances of the corrected, non-hydrostatic, GEM10B geoid.

$$\delta^2_{rms} = \frac{1}{4\pi} \int_0^{2\pi} \int_{-1}^{1} \left[G_p(\theta,\phi) - G_o(\theta,\phi) \right]^2 d\cos\theta \, d\phi \,, \tag{33}$$

where $G_p(\theta,\phi)$ and $G_o(\theta,\phi)$ are, respectively, the predicted and observed non-hydrostatic

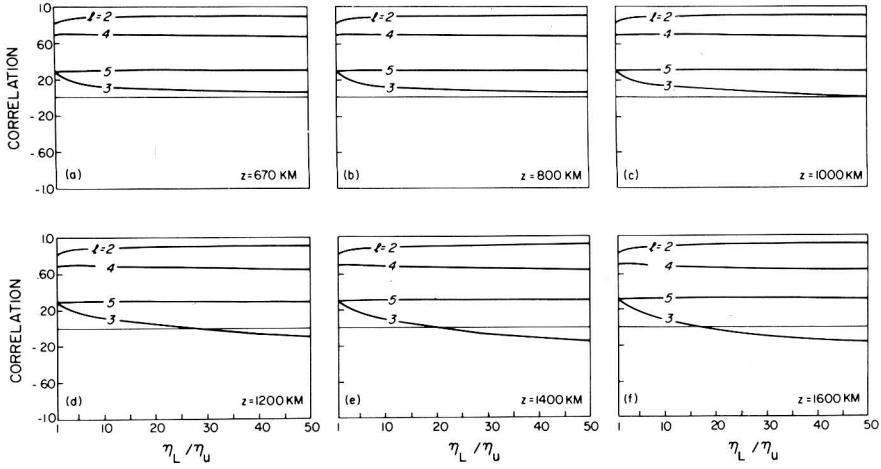

Figure 10. Degree correlations of the observed and predicted surface divergence fields for a two-layer mantle, as a function of viscosity contrast and depth of viscosity jump.

geoids. Expanding both G_p and G_o in terms of spherical harmonics one then obtains from (33),

$$\delta^2_{rms} = \sum_l \delta^2_l \,, \tag{34}$$

where,

$$\delta^2_l = (\sigma_p)^2_l + (\sigma_o)^2_l - 2\rho_l\,(\sigma_p)_l\,(\sigma_o)_l$$

In (34), $(\sigma_p)_l$ and $(\sigma_o)_l$ are the degree variances of the predicted and observed non-hydrostatic geoid, respectively, while ρ_l is the degree correlation between these two fields. When the depth of the boundary between the layers is at z = 670 km, the rms errors obtained for the case $\eta_L/\eta_u = 18$ (which maximizes the degree correlations) and for the case $\eta_L/\eta_u = 6$ (which best matches all the degree variances) are presented in Table 3. In Table 4 are shown the rms errors when z = 1200 km for the cases $\eta_L/\eta_u = 8$ (maximizes degree correlations) and $\eta_L/\eta_u = 4$ (matches the degree variances). A comparison of these two tables show that a sort of "trade-off" exists in that essentially equivalent fits (as measured by δ_{rms}) to the observed non-hydrostatic geoid are obtained by either placing the boundary at z = 670 km with $\eta_L/\eta_u = 18$ or by placing it deeper, at z = 1200 km, which then requires a lower viscosity ratio of $\eta_L/\eta_u = 8$. The slightly better fit to the observed non-hydrostatic geoid in the range l = 2-5 when z = 1200 km and $\eta_L/\eta_u = 8$ is entirely due to the much improved fits at l = 4 and 5 compared to when z = 670 km. A more graphic illustration of the extent to which the predicted geoid matches the observed non-hydrostatic geoid for the case z = 1200 km and $\eta_L/\eta_u = 8$ is provided in Fig. 11.

Now that the optimum viscosity ratio and boundary depth have been determined, the absolute value of the mantle viscosity may be found by matching the kinetic energy of the

Table 3 Rms errors between predicted and observed non-hydrostatic geoid for the case z = 670 km.

$\eta_L/\eta_u = 18$

Degree, l	$(\sigma_p)_l$ (metres)	ρ_l	δ_l (metres)
l=2	15.8	.82	19.8
l=3	15.2	.87	10.0
l=4	13.6	.25	14.8
l=5	16.3	-.52	21.2
	δ_{rms} = 34.1 m		

$\eta_L/\eta_u = 6$

Degree, l	$(\sigma_p)_l$ (metres)	ρ_l	δ_l (metres)
l=2	28.0	.13	38.7
l=3	22.8	.67	17.5
l=4	8.8	-.48	16.4
l=5	9.7	.53	8.6
	δ_{rms} = 46.3 m		

predicted, purely poloidal, surface flow field to the kinetic energy of the observed surface plate velocities which consist of both poloidal and toroidal components. We include the kinetic energy of the toroidal field since we assume that it is produced by a flux of energy out of the poloidal field. The amplitude of the predicted horizontal divergence (or, equivalently, of the predicted poloidal scalar; cf. (3a)) depends on both η_L/η_u and η_u and to illustrate this dependence in a single diagram we have plotted in Fig. 12 a quantity called $\log_{10}(\sigma_R)$ which is defined by:

$$\log_{10}(\sigma_R) = \log_{10}\left[\frac{\sigma_l(\eta_L/\eta_u)}{\sigma_l(\eta_L/\eta_u=1)}\right], \tag{35}$$

where $\sigma_l(\eta_L/\eta_u)$ is the degree of the predicted horizontal divergence for a given value of η_L/η_u. The quantity σ_R defined in (35) will be independent of η_u since this viscosity appears merely as a multiplicative factor in (31) and thus $\log_{10}(\sigma_R)$ is only a function of η_L/η_u. The observational constraints on η_u (and hence η_L) are introduced by considering

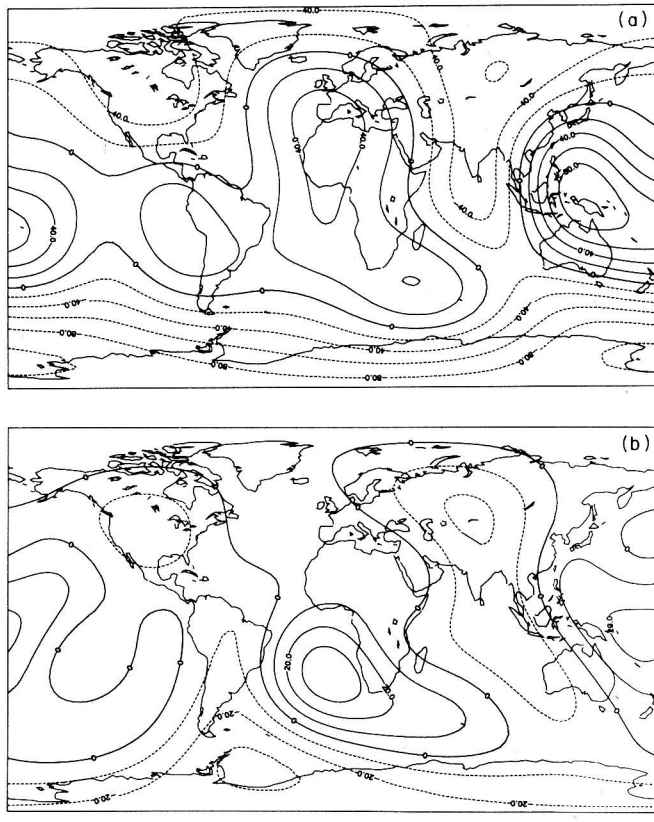

Figure 11. (a) The corrected, non-hydrostatic, GEM10B geoid synthesized from harmonics in the range $2 \leq l \leq 5$. The contour interval is 20 metres. (b) The non-hydrostatic geoid predicted using the geoid kernel for a two-layer, self-gravitating mantle with a factor of eight viscosity increase at a depth of 1200 km. The contour interval is 10 metres.

$$\log_{10}(\sigma_o) = \log_{10}\left[\frac{\sigma_l(\text{observed})}{\sigma_l(\eta_l/\eta_u=1)}\right], \tag{36}$$

where σ_l(observed) is the total kinetic energy (i.e. poloidal + toroidal), at each degree, of the observed surface plate velocities. The quantity σ_o, defined in (36), is directly proportional to η_u and is independent of η_L/η_u. The horizontal dashed lines in Fig. 12 are plots of $\log_{10}(\sigma_o^*)$ for $\eta_u^* = 1 \times 10^{21}$ Pa s. When an appropriate value for η_L/η_u has been found then the value of η_u is determined by equating $\log_{10}(\sigma_R)$ with $\log_{10}(\sigma_o)$ and in Fig. 12 this is equivalent to measuring, for a particular degree, the distance as measured along the ordinate axis of the point (determined by η_L/η_u) on a $\log_{10}(\sigma_R)$ curve from the $\log_{10}(\sigma_o^*)$ line ; if this distance is called d then the value of η_u is $\eta_u = 10^d \times \eta_u^* = 10^d \times 10^{21}$ Pa s. Now, since the best degree correlations between the predicted and observed

Table 4 Rms errors between predicted and observed non-hydrostatic geoid for the case z = 1200 km.

$\eta_L/\eta_u = 8$

Degree, l	$(\sigma_p)_l$ (metres)	ρ_l	δ_l (metres)
l=2	8.4	.78	24.6
l=3	5.0	.65	17.1
l=4	3.0	.13	10.3
l=5	5.8	.53	6.6
	δ_{rms} = 32.3 m		

$\eta_L/\eta_u = 4$

Degree, l	$(\sigma_p)_l$ (metres)	ρ_l	δ_l (metres)
l=2	22.1	.11	35.7
l=3	14.6	.59	16.3
l=4	7.8	-.47	15.5
l=5	13.3	.62	10.5
	δ_{rms} = 43.5 m		

horizontal divergence fields are at l = 2 and 4, we will match the predicted and observed kinetic energies at these same two degrees in the manner just described. We find then that for the case z = 670 km and η_L/η_u = 18 the value of η_u determined from the degree-2 matching is 1.47 x 10^{21} Pa s which agrees well with η_u = 1.55 x 10^{21} Pa s determined from the degree-4 matching. When z = 1200 km and η_L/η_u = 8, the value of η_u determined from l = 2 is 2.31 x 10^{21} Pa s which again agrees well with η_u = 2.26 x 10^{21} Pa s obtained from l = 4.

The predicted and observed horizontal divergence fields are well-correlated at l = 2 and 4 as noted previously. A more pictoral illustration of the agreement between these two fields is given in Fig. 13 where we show maps of the predicted and observed horizontal divergence synthesized from harmonics in the range l = 2-5. The agreement between these maps is quite good and the places where the biggest mismatch occur are North America, Asia and Australia; these regions are incorrectly shown to be subducting in the predicted divergence map since our simple model does not incorporate the effects of lateral variations in chemistry which produce buoyant continental masses.

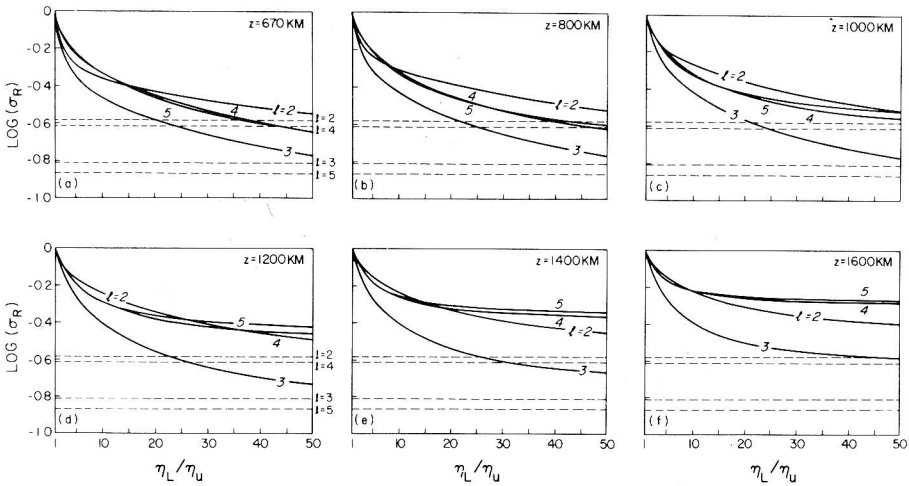

Figure 12. Degree variances of the predicted surface divergence field, for a two-layer mantle, as measured by log (σ_R) (cf. equation (35)) as a function of viscosity contrast and depth of viscosity jump. The dashed horizontal lines are the degree variances of the observed surface divergence field, as measured by log (σ_o) (cf. equation (36)).

4. The importance of poloidal-toroidal coupling

The agreement between the predicted and observed fields in the maps shown in Figs. 11 and 13 is encouraging and it illustrates the approximate validity of the very simple viscous flow models that we have used. It is certain that an improved fit to the observed surface fields may be made by increasing the accuracy and resolution of the seismically inferred lateral heterogeneity models that we have used. However, the most serious problem with our spherically symmetric viscosity models is that lateral density variations will only force a purely poloidal flow field. We are therefore unable to reproduce the observed equipartition of kinetic energy between the poloidal and toroidal flows at the Earth's surface. Toroidal flows may be generated by allowing the viscosity to vary laterally thus producing a coupling between poloidal and toroidal scalars (Forte and Peltier, in preparation). We expect that this coupling will be strongest in the lithosphere-asthenosphere where the lateral variations of rheology and chemistry are the most extreme.

An Earth model with poloidal-toroidal coupling is expected to produce geoids that are quite different from those presented in this report. The predicted geoid depends almost entirely on the fine balance achieved between the opposing contributions from the surface topography and the internal mass anomalies. The good geoid correlations obtained with the two-layer model are a direct result of the reduced surface topography produced by increasing the viscosity of the lower layer. If one introduces lateral viscosity/chemistry variations then we expect that a similar reduction in topography might be achieved since we assume that the toroidal flow that is generated in the near-surface region at the expense of the interior poloidal flow will itself produce little or no surface topography while the topography supported by the now weaker, near-surface, poloidal flow will be diminished.

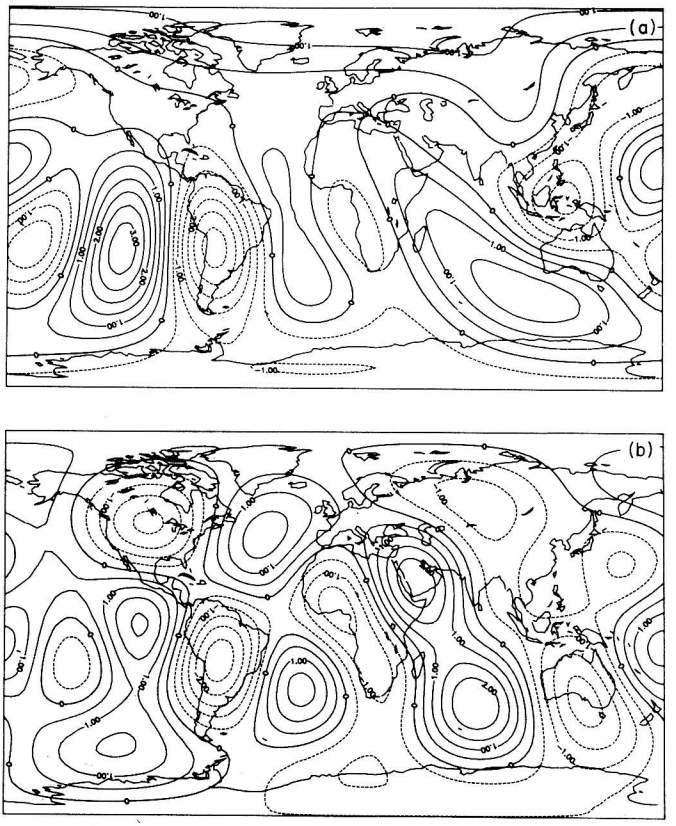

Figure 13. (a) The normalized, observed horizontal divergence of the surface plate motions synthesized from harmonics in the range $2 \leq l \leq 5$. This field has been normalized by dividing by the total degree variance of the actual field for the range $2 \leq l \leq 5$ such that the total degree variance of the field shown in the map is exactly unity. The contour interval is 0.5 (dimensionless units). (b) The normalized horizontal divergence predicted using the divergence kernel for a two-layer mantle with a factor of eight viscosity increase at a depth of 1200 km. This field has also been normalized as in (a). The normalized, predicted divergence field depends only on η_L/η_u and is independent of η_u (cf. equation (31)) thus facilitating a direct comparison with the field shown in (a). The contour interval is 0.5 (dimensionless units).

This suggests then that one may model the geoid with smaller viscosity increases at depth by introducing lateral viscosity/chemistry variations in the near surface region. The trade-off between poloidal-toroidal coupling and the strength of the viscosity contrast in the two-layer model may be illustrated in a somewhat ad hoc manner by defining a "poloidal conversion factor", α. We may then try to reproduce the effect of poloidal-toroidal conversion near the Earth's surface by multiplying the poloidal scalar, $p_l^m(r=a)$, by α thus simulating a $(1 - \alpha^2)$ x 100% flux of energy to a toroidal flow which we assume contributes little or nothing to the geoid. In Fig. 14(a) and (d) we show, for example, that a great improvement in the $l = 2$ geoid correlation is obtained when $\alpha = 0.875$. In Table 5 we

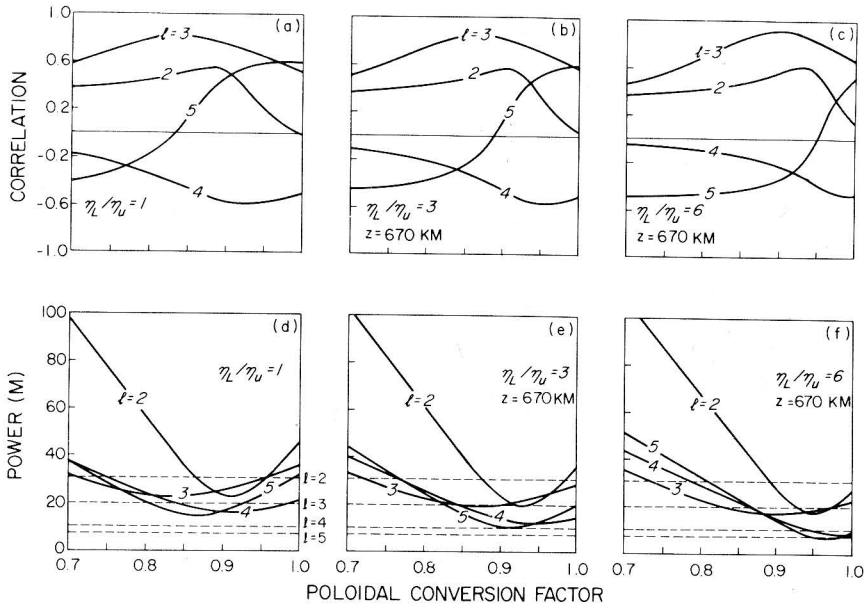

Figure 14. Behaviour of the predicted geoid when the effect of poloidal-toroidal coupling at the surface is simulated via a poloidal conversion factor. A conversion factor, α, mimics a $(1 - \alpha^2) \times 100\%$ flux of energy to the toroidal field: (a), (b) and (c) Degree correlations of corrected, non-hydrostatic, GEM10B geoid with predicted geoid as a function of α; (d), (e) and (f) degree variances (in metres) of predicted geoid as a function of α. Dashed horizontal lines are degree variances of corrected, non-hydrostatic, GEM10B geoid.

show that the good match between the predicted and observed geoid at $l = 2$ for $\eta_L/\eta_u = 20$ is due to the reduction of the surface topography at this degree from 695 m to 538 m and that a similar reduction is achieved in a constant viscosity mantle with a 23% flux of energy to the toroidal field.

5. Concluding remarks

The Green function formalism provides a mathematically straightforward method for deriving analytic, closed-form, expressions for the kernel functions relating the horizontal divergence of the surface flow and the non-hydrostatic geoid to the seismic tomographic inferences of lateral density variations in the mantle. The kernel functions for a two-layer mantle were used to predict horizontal divergence and non-hydrostatic geoid fields which are in fairly good agreement with the corresponding observed fields. In particular, we have shown that the agreement between the predicted and observed horizontal divergence fields (cf. Fig. 13) is reasonably good thus providing strong support to the notion that the large-scale tectonic plate motions are the direct expression of the convective flow in the mantle driven by internal thermally induced buoyancy forces.

A central aim of this report has been to present a unified description of both the non-hydrostatic geoid and the surface plate kinematics as represented by the horizontal

Table 5 Degree variances of the predicted surface topography

$\alpha = 1.0, \eta_L/\eta_u = 1$

Degree, l	Degree variance (metres)
l=2	695
l=3	449
l=4	582
l=5	1,012

$\alpha = 1.0, \eta_L/\eta_u = 20$, z = 670 km

Degree, l	Degree variance (metres)
l=2	538
l=3	342
l=4	452
l=5	753

$\alpha = 0.875, \eta_L/\eta_u = 1$

Degree, l	Degree variance (metres)
l=2	542
l=3	371
l=4	486
l=5	856

divergence field. The predicted non-hydrostatic geoid depends only on the viscosity ratio in a two-layer Earth model but the predicted horizontal divergence instead depends on the absolute values of the viscosity in each layer. We have thus been able to establish preliminary estimates of the absolute value of the viscosity by ensuring that the balance between buoyancy forces and viscous dissipation is such as to produce a surface flow whose kinetic energy matches that of the observed surface plate velocities. In attempting to match the predicted and observed non-hydrostatic geoids we found that a trade-off exists between the required viscosity contrast and the depth of the viscosity jump in the two-layer model. We found further that the two-layer model providing the most successful fit to the observed non-hydrostatic geoid has a factor of eight viscosity increase at a depth of 1200 km; in this model the viscosity of the upper layer is $\eta_u = 2.3 \times 10^{21}$ Pa s while that of the

lower layer is $\eta_L = 1.8 \times 10^{22}$ Pa s. The discrepancy between these preliminary viscosity estimates and those obtained from post-glacial rebound (e.g. Wu and Peltier, 1983) may have implications for the issue of transient rheology in the mantle (Peltier et al., 1986; Forte and Peltier, 1986).

The existence of strong toroidal flow in the observed surface plate velocities points to an important defect in Earth models with a spherically-symmetric viscosity distribution since such models are unable to produce any toroidal flow. In section 4 we argued that the generation of toroidal flow by a flux of energy out of the poloidal flow field is likely to produce surface topography of smaller amplitude than that produced in the absence of this effect. Since the predicted geoid is very strongly dependent on the predicted surface topography we then believe that incorporation of the effects of poloidal-toroidal coupling may allow us to fit the predicted geoid to the observed geoid with a smaller viscosity increase at depth in the mantle thus providing a possible reconciliation with the small viscosity contrast at the 670 km seismic discontinuity required by glacial isostatic adjustment analyses. If such a reconciliation were not possible then it may be necessary to argue that the viscosity inferences obtained from glacial isostatic adjustment analyses represent transient values rather than steady-state values (Peltier et al., 1986).

Appendix A: Homogeneous, incompressible mantle

A.1 *Derivation of the Green function*

The required Green function must satisfy equation (17); that is,

$$D_l^2\, p_l^m(r,r') = \delta(r-r')\,. \tag{A1}$$

When $r \neq r'$, (A1) is the biharmonic equation whose solution is easily found; therefore, the solution of (A1) is split in two parts: a solution defined for the region $r' < r \leq a$ and a solution for the region $b \leq r < r'$. These two solutions must then be joined at $r=r'$ by applying the appropriate matching conditions. The biharmonic equation,

$$D_l^2\, p_l^m(r,r') = 0\,,$$

is a fourth order differential equation whose solution will consist of the sum of four linearly independent functions:

$$p_l^m(r,r') = A_1 r^l + \frac{B_1}{r^{l+1}} + C_1 r^{l+2} + \frac{D_1}{r^{l-1}}\,, \quad r' < r \leq a$$

$$p_l^m(r,r') = A_2 r^l + \frac{B_2}{r^{l+1}} + C_2 r^{l+2} + \frac{D_2}{r^{l-1}}\,, \quad b \leq r < r' \tag{A2}$$

In (A2) there are 8 coefficients which are found by applying the boundary conditions at $r=a$, $r=b$ and the matching conditions at $r=r'$. Two boundary conditions are obtained by requiring that the radial component of the fluid velocity, u_r, is zero at the deformed bounding surfaces of the fluid layer (which to first order accuracy may be taken as applying

at the undeformed reference positions of the bounding surfaces):

$$u_r = \hat{\mathbf{r}}\cdot\mathbf{u} = \frac{1}{r}\,\Lambda^2 p \tag{A3}$$

Therefore, from (A3), one sees that if $u_r = 0$ for all θ and ϕ at both $r=a$ and $r=b$, then

$$p_l^m(r,r') = 0 \ , \ r=a,b \tag{A4}$$

Two more boundary conditions are obtained by requiring that the shear stresses, $\sigma_{r\theta}$ and $\sigma_{r\phi}$, are both zero at $r=a$ and $r=b$, and one may show (e.g., Chandrasekhar, 1961) this condition implies that

$$\frac{d^2}{dr^2}\,p_l^m(r,r') = 0 \ , \ r=a,b \tag{A5}$$

Three matching conditions are obtained by requiring that u_r, u_θ (and u_ϕ), and $\sigma_{r\theta}$ (and $\sigma_{r\phi}$) are continuous at $r=r'$; one can therefore show that:

$$p_l^m(r,r')\big|_{r=r'^+} = p_l^m(r,r')\big|_{r=r'^-} ,$$

$$\frac{dp_l^m(r,r')}{dr}\Big|_{r=r'^+} = \frac{dp_l^m(r,r')}{dr}\Big|_{r=r'^-} , \tag{A6}$$

$$\frac{d^2p_l^m(r,r')}{dr^2}\Big|_{r=r'^+} = \frac{d^2p_l^m(r,r')}{dr^2}\Big|_{r=r'^-} .$$

The final matching condition is obtained by integrating equation (A1) from $r=r'^-$ to $r=r'^+$ and using (A6) to obtain

$$\frac{d^3p_l^m(r,r')}{dr^3}\Big|_{r=r'^+} - \frac{d^3p_l^m(r,r')}{dr^3}\Big|_{r=r'^-} = 1 \tag{A7}$$

The eight conditions contained in equations (A4), (A5), (A6) and (A7) when applied to (A2) will yield expressions for the 8 coefficients:

$$A_1 = -\frac{D_1}{a^{2l-1}} \ , B_1 = -C_1\,a^{2l+3}$$

$$C_1 = \frac{1}{2(2l+3)(2l+1)}\,\frac{1}{r'^{l-1}}\,\frac{1-(r'/b)^{2l+3}}{1-(a/b)^{2l+3}} \tag{A8}$$

$$D_1 = \frac{1}{2(4l^2-1)}\,\frac{a^{2l-1}}{r'^{l-3}}\,\frac{1-(r'/b)^{2l-1}}{1-(a/b)^{2l-1}}$$

and

$$A_2 = -\frac{D_2}{b^{2l-1}}, B_2 = -C_2 b^{2l+3}$$

$$C_2 = -\frac{1}{2(2l+3)(2l+1)} \frac{1}{r'^{l-1}} \frac{1-(r'/a)^{2l+3}}{1-(b/a)^{2l+3}} \tag{A9}$$

$$D_2 = -\frac{1}{2(4l^2-1)} \frac{b^{2l-1}}{r'^{l-3}} \frac{1-(r'/a)^{2l-1}}{1-(b/a)^{2l-1}}$$

In order to obtain expressions for the kernel functions describing surface divergence and geoid height one requires expressions for the derivatives of the poloidal scalar which is given by equation (18), that is,

$$p_l^m(r) = \frac{g_o}{\eta} \left[\int_r^a \frac{(\rho_1)_l^m(r')}{r'} (p_2)_l^m(r,r') dr' \right.$$

$$\left. + \int_b^r \frac{(\rho_1)_l^m(r')}{r'} (p_1)_l^m(r,r') dr' \right] \tag{A10}$$

where $(p_1)_l^m(r,r')$ is the Green function valid for $r' \le r \le a$ and $(p_2)_l^m(r,r')$ is the Green function valid for $b \le r < r'$ (see equation (A2)). From expression (A10) one may readily show that the Green functions for the first, second, and third derivatives of $p_l^m(r)$ are the first, second, and third derivatives of $p_l^m(r,r')$ respectively.

A.2. *The surface divergence kernel*

Since $\nabla \cdot \mathbf{u} = 0$, then

$$\nabla_H \cdot \mathbf{u} = -\frac{1}{r^2} \frac{\partial}{\partial r} (r^2 u_r) \tag{A11}$$

Now, to first-order accuracy, $u_r = 0$ at $r=a$ and therefore from (A11) we get

$$\nabla_H \cdot \mathbf{u}(r=a) = -\frac{\partial u_r}{\partial r}\Big|_{r=a} \tag{A12}$$

If one substitutes (A3) into (A12), expands into spherical harmonics, and uses result (A4) then one can show that

$$(\nabla_H \cdot \mathbf{u})_l^m(r=a) = \frac{l(l+1)}{a} \frac{dp_l^m(r)}{dr}\Big|_{r=a} . \tag{A13}$$

Result (A13) proves equation (3a). From (A10) one gets

$$\frac{dp_l^m(r)}{dr}\Big|_{r=a} = \frac{g_o}{\eta} \int_b^a \frac{(\rho_1)_l^m(r')}{r'} \frac{d(p_1)_l^m(r,r')}{dr}\Big|_{r=a} dr' \tag{A14}$$

Upon substituting (A2) into (A14), and using (A8), one finds from (A13) that

$$(\nabla_H \cdot \mathbf{u})_l^m(r=a) = \frac{g_o}{\eta} \int_b^a S_l(r')\,(\rho_1)_l^m(r')\,dr' ,$$

where

$$S_l(r') = \frac{a^l l(l+1)}{2(2l+1)} \left[\frac{1}{r'^l} \frac{1-(r'/b)^{2l+3}}{1-(a/b)^{2l+3}} - \frac{1}{a^2 r'^{l-2}} \frac{1-(r'/b)^{2l-1}}{1-(a/b)^{2l-1}} \right] .$$

A.3. *The Geoid Kernel*

If one expands all quantities in equation (25) in terms of spherical harmonics then the following result is obtained

$$\delta a_l^m = \frac{1}{g_o(\rho_o - \rho_w)} \left[(P_1)_l^m(r=a) - 2\eta \left. \frac{d(u_r)_l^m(r)}{dr} \right|_{r=a} \right] . \tag{A15}$$

The non-hydrostatic pressure may be obtained from the $\hat{\theta}$-component of the momentum equation (6):

$$\frac{1}{r} \frac{\partial}{\partial \theta} P_1 = \eta \left[\Delta \mathbf{u} \right]_\theta + \rho_o \frac{1}{r} \frac{\partial \phi_1}{\partial \theta} ,$$

where one can show from (10), assuming a purely poloidal flow field, that

$$\left[\Delta \mathbf{u} \right]_\theta = -\frac{1}{r} \frac{\partial}{\partial \theta} \frac{\partial}{\partial r} r \Delta p ,$$

and thus if one expands all quantities in terms of spherical harmonics one can show that

$$(P_1)_l^m = -\eta \frac{d}{dr} \left[r D_l p_l^m(r) \right] + \rho_o (\phi_1)_l^m , \tag{A16}$$

where D_l is the transformed Laplacian operator in equation (15). Now, from (A3) it follows that

$$(u_r)_l^m(r) = -\frac{1}{r} l(l+1)\, p_l^m(r) . \tag{A17}$$

If (A16) and (A17) are substituted into (A15), and use is made of the boundary conditions (A4) and (A5), it follows that

$$\delta a_l^m = \frac{1}{(\rho_o - \rho_w)} X_l^m(r=a) + \frac{\rho_o}{g_o(\rho_o - \rho_w)} (\phi_1)_l^m(r=a) , \tag{A18}$$

where

$$X_l^m(r) = \frac{\eta}{g_o} \left[-r \frac{d^3}{dr^3} + \frac{3l(l+1)}{r} \frac{d}{dr} \right] p_l^m(r) \tag{A19}$$

Similarly, in the case of the core-mantle boundary deflection, δb_l^m, one can show that

$$\delta b_l^m = \frac{1}{(\rho_o - \rho_c)} X_l^m(r=b) + \frac{\rho_o}{g_o(\rho_o - \rho_c)} (\phi_1)_l^m(r=b) . \tag{A20}$$

If one now substitutes (A18) into (22), (A20) into (23), and combines the results in (24) then one may show that

$$(\phi_1)_l^m(r) = (U_{int})_l^m(r) + \frac{4\pi aG}{2l+1}\left[\frac{r}{a}\right]^l \left[X_l^m(r=a) + \frac{\rho_o}{g_o}(\phi_1)_l^m(r=a)\right]$$

$$- \frac{4\pi bG}{2l+1}\left[\frac{b}{r}\right]^{l+1}\left[X_l^m(r=b) + \frac{\rho_o}{g_o}(\phi_1)_l^m(r=b)\right] \tag{A21}$$

In equation (A21) it is clear that to find $(\phi_1)_l^m(r)$ one must know $(\phi_1)_l^m(r=a)$ and $(\phi_1)_l^m(r=b)$; this is easily accomplished by setting $r=a$ and $r=b$ in (A21) thus producing two simultaneous equations which may be solved to find $(\phi_1)_l^m(r=a)$ and $(\phi_1)_l^m(r=b)$ and having done this one may then show that

$$(\phi_1)_l^m(r) = (U_{int})_l^m(r) + \left[\frac{r}{a}\right]^l \left[(1-K_a)(1+K_b) + K_a K_b \left[\frac{b}{a}\right]^{2l+1}\right]^{-1}$$

$$\left\{\left[1 + K_b\left[1 - \left[\frac{b}{r}\right]^{2l+1}\right]\right]\left[K_a (U_{int})_l^m(r=a) + \frac{4\pi aG}{2l+1} X_l^m(r=a)\right] -\right.$$

$$\left.\left[\frac{b}{a}\right]^{l+1}\left[K_a\left[1 - \left[\frac{a}{r}\right]^{2l+1}\right] + \left[\frac{a}{r}\right]^{2l+1}\right]\left[K_b (U_{int})_l^m(r=b) + \frac{4\pi bG}{2l+1} X_l^m(r=b)\right]\right\} , \tag{A22}$$

where

$$K_a = \frac{4\pi aG}{2l+1}\frac{\rho_o}{g_o} \text{ and } K_b = \frac{4\pi bG}{2l+1}\frac{\rho_o}{g_o} . \tag{A23}$$

When expression (A19) is substituted into (A22) one may show that

$$(\phi_1)_l^m(a) = \frac{4\pi aG}{2l+1}\int_b^a G_l(r')\,(\rho_1)_l^m(r')\,dr' , \tag{A24}$$

where

$$G_l(r') = \left[1 - K_a + \frac{K_a K_b}{1+K_b}\left[\frac{b}{a}\right]^{2l+1}\right]^{-1}\left[\frac{r'}{a}\right]^{l+2}\left\{1 - \frac{K_a}{1+K_b}\left[\frac{b}{r'}\right]^{2l+1}\left[\frac{b}{a}\right] +\right.$$

$$\left. A_l(r')\left[1 - \frac{K_a}{1+K_b}\left[\frac{b}{a}\right]^{2l+2}\right]\left[\frac{a}{r'}\right]^{l+2} - B_l(r')\left[1 - \frac{K_a}{1+K_b}\left[\frac{b}{a}\right]\right]\left[\frac{b}{r'}\right]^{l+2}\right\}, \tag{A25}$$

and where

$$A_l(r') = -\frac{l(l+2)}{2l+1}\left[\frac{a}{r'}\right]^{l-2}\frac{1-(r'/b)^{2l-1}}{1-(a/b)^{2l-1}} + \frac{(l+1)(l-1)}{2l+1}\left[\frac{a}{r'}\right]^{l}\frac{1-(r'/b)^{2l+3}}{1-(a/b)^{2l+3}},$$

$$B_l(r') = \frac{l(l+2)}{2l+1}\left[\frac{b}{r'}\right]^{l-2}\frac{1-(r'/a)^{2l-1}}{1-(b/a)^{2l-1}} - \frac{(l+1)(l-1)}{2l+1}\left[\frac{b}{r'}\right]^{l}\frac{1-(r'/a)^{2l+3}}{1-(b/a)^{2l+3}}.$$

The non-hydrostatic geoid-height field is obtained from $\phi_1(r=a)$ by dividing by g_o and thus from (A24) one has

$$(Ge)_l^m = \frac{3}{2l+1}\frac{1}{\bar{\rho}}\int_b^a G_l(r')\,(\rho_1)_l^m(r')\,dr',$$

where $(Ge)_l^m$ is the harmonic coefficient of the geoid-height field, $\bar{\rho}$ is the average density of the Earth, and $G_l(r')$ is the geoid kernel given in equation (A25).

The effects of self-gravitation on the geoid are contained in the constants K_a and K_b which are defined in equation (A23). To obtain the geoid kernels, $G_l(r')$, for a non-self-gravitating mantle one simply sets both K_a and K_b to be zero in equation (A25); one may also note that this equivalent to letting $l \to \infty$.

Appendix B: Inhomogeneous (two-layer), incompressible mantle

B.1 *Derivation of the Green function*

As in equation (A2), the Green function $(p_i)_l^m(r,r')$, valid in region i (i = 1,2,3,4,5, and 6 - see Fig. 5 and equation (30)) is given by the expression

$$(p_i)_l^m(r,r') = A_i\, r^l + \frac{B_i}{r^{l+1}} + C_i\, r^{l+2} + \frac{D_i}{r^{l-1}}. \qquad \text{(B1)}$$

For either case (i) or case (ii) (Fig. 5) equation (B1) shows there are 12 coefficients to be found; they are determined by applying the free-slip boundary conditions at $r=a$ and b, matching conditions at $r=r'$ (see Appendix A), and by applying appropriate matching conditions at $r=d$. Since we assume that a whole mantle flow exists the conditions we impose at $r=d$ are continuity of mass flux, normal stress, tangential stress, and tangential velocity:

$$\rho_u \, u_r \big|_{r=d^+} = \rho_L \, u_r \big|_{r=d^-} , \tag{B2a}$$

$$\sigma_{rr} \big|_{r=d^+} - \sigma_{rr} \big|_{r=d^-} = (\rho_L - \rho_u) \, g_o \, \delta d , \tag{B2b}$$

$$\sigma_{r\theta} \big|_{r=d^+} = \sigma_{r\theta} \big|_{r=d^-} , \tag{B2c}$$

$$u_\theta \big|_{r=d^+} = u_\theta \big|_{r=d^-} , \tag{B2d}$$

where ρ_u and ρ_L are, respectively, the densities of the upper and lower layers and δd is the deflection of the material interface $r=d$ from its reference level. A considerable simplification is made by assuming, as in Richards and Hager (1984), that $\rho_u = \rho_L$ (= 4.43 g/cm^3) since then we can ignore the deflection δd in equation (B2b). When the 12 boundary and matching conditions are applied to (B1) one may find all the coefficients; expressions for these coefficients may be found in Forte and Peltier (1986).

B.2 *The surface divergence kernel*

To determine the surface divergence field in a two-layered mantle we again use equation (A13) in Appendix A. The radial derivative of the poloidal scalar at $r=a$ is obtained from expression (30a):

$$\frac{dp_l^m}{dr} \Big|_{r=a} = \frac{g_o}{\eta_u} \int_d^a \frac{d\,(p_4)_l^m(r,r')}{dr} \Big|_{r=a} \frac{(\rho_1)_l^m(r')}{r'} \, dr' +$$

$$\frac{g_o}{\eta_L} \int_b^d \frac{d\,(p_3)_l^m(r,r')}{dr} \Big|_{r=a} \frac{(\rho_1)_l^m(r')}{r'} \, dr' \tag{B3}$$

Using expression (B1) one can show, using (A13) with (B3), that

$$(\nabla_H \cdot \mathbf{u})_l^m(r=a) = \frac{g_o}{\eta_u} \int_b^a S_l(r';\gamma,d) \, (\rho_1)_l^m(r') \, dr' , \tag{B4}$$

where $\gamma = \eta_L / \eta_u$,

$$S_l(r';\gamma,d) = \begin{cases} p'(4) , & d \le r' \le a \\ \dfrac{1}{\gamma} \, p'(3) , & b \le r' \le d \end{cases}$$

where,

$$p'(i) = l(l+1)\left[-l\left(\frac{a}{r'}\right)A_i' + (l+1)\left(\frac{a}{r'}\right)B_i' + (l+2)\left(\frac{a}{r'}\right)^{l} C_i' - (l-1)\left(\frac{r'}{a}\right)^{l+1} D_i'\right].$$

The quantities A_i', B_i', C_i', and D_i' are obtained by non-dimensionalizing the coefficients A_i, B_i, C_i, D_i according to:

$$A_i' = -a^{l-3}A_i,\ B_i' = -\frac{1}{a^{l+4}}B_i,\ C_i' = r'^{l-1}C_i,\ D_i' = \frac{1}{r'^{l+2}}D_i\ .$$

B.3 *The geoid kernel*

In our two-layer model we have assumed, for simplicity, that the densities of the upper and lower layers are equal and therefore any deflection of the interface $r=d$ will not affect the perturbed potential ϕ_1; consequently, equation (A22) of Appendix A will also be valid for the two-layered Earth. The first task is thus to determine the kernels for the quantities $X_l^m(r=a)$ and $X_l^m(r=b)$. From equation (A19) we have

$$X_l^m(r=a) = \frac{\eta_u}{g_o}\left[-r\frac{d^3}{dr^3} + \frac{3l(l+1)}{r}\frac{d}{dr}\right] p_l^m(r)\Big|_{r=a}\ , \tag{B5a}$$

$$X_l^m(r=b) = \frac{\eta_L}{g_o}\left[-r\frac{d^3}{dr^3} + \frac{3l(l+1)}{r}\frac{d}{dr}\right] p_l^m(r)\Big|_{r=b}\ . \tag{B5b}$$

If one substitutes (30a) into (B5a) then the following expression is obtained:

$$X_l^m(r=a) = \int_b^a K_l^a(r')\,(\rho_1)_l^m(r')dr'\ , \tag{B6}$$

where,

$$K_l^a(r') = \begin{cases} p_1''(4)\ , & d \le r' \le a \\ \dfrac{1}{\gamma}\,p_1''(3)\ , & b \le r' \le d \end{cases}$$

where

$$p_1''(i) = 2\left[-l(l^2+3l-1)\left(\frac{a}{r'}\right)A_i' + (l+1)(l^2-l-3)\left(\frac{a}{r'}\right)B_i' + l(l+1)(l+2)\left(\frac{a}{r'}\right)^{l} C_i' - l(l+1)(l-1)\left(\frac{r'}{a}\right)^{l+1} D_i'\right].$$

The quantities, A_i', B_i', C_i', and D_i' appearing in the expression for $p_1''(i)$ have the same

definition as those in $p'(i)$. Similarly, if one substitutes (30b) into (B5b) it can be shown that

$$X_l^m(r=b) = \int_b^a K_l^b(r')\,(\rho_1)_l^m(r')\,dr' \,, \tag{B7}$$

where,

$$K_l^b(r') = \begin{cases} \gamma p_2''(6), & d \le r' \le a \\ p_2''(2), & b \le r' \le d \end{cases}$$

where

$$p_2''(i) = 2\left[-l(l^2+3l-1)\left[\frac{b}{r'}\right]A_i' + (l+1)(l^2-l-3)\left[\frac{b}{r'}\right]B_i' + \right.$$

$$\left. l(l+1)(l+2)\left[\frac{b}{r'}\right]^l C_i' - l(l+1)(l-1)\left[\frac{r'}{b}\right]^{l+1} D_i'\right] .$$

The quantities A_i', B_i', C_i', D_i' appearing in the expression for $p_2''(i)$ are now defined according to:

$$A_i' = -b^{l-3}A_i, B_i' = -\frac{1}{b^{l+4}}B_i, C_i' = r'^{l-1}C_i, D_i' = \frac{1}{r'^{l+2}}D_i \,.$$

If one sets $r=a$ in equation (A22), and substitutes (B6) and (B7) into the resulting equation, the following expression for the self-gravitating potential is obtained:

$$(\phi_1)_l^m(a) = \frac{4\pi aG}{2l+1}\int_b^a G_l(r';\gamma,d)\,(\rho_1)_l^m(r')\,dr' \,, \tag{B8}$$

where,

$$G_l(r';\gamma,d) = \left[\frac{r'}{a}\right]^{l+1}\left\{1+\left[(1-K_a)(1+K_b)+K_aK_b\left[\frac{b}{a}\right]^{2l+1}\right]^{-1}\left[\left[1+K_b\left[1-\left[\frac{b}{a}\right]^{2l+1}\right]\right]\right.\right.$$

$$\left.\left.\cdot\left[K_a+\left[\frac{a}{r'}\right]^{l+2}K_l^a(r')\right]-\left[\frac{b}{r'}\right]^{l+2}\left[K_b\left[\frac{b}{r'}\right]^{l-1}+K_l^b(r')\right]\right]\right\}, \tag{B9}$$

where the constants K_a and K_b are defined in equation (A23). The spherical harmonic coefficients of the non-hydrostatic geoid $(Ge)_l^m$ are directly obtained from (B8) by dividing by g_o:

$$(Ge)_l^m = \frac{3}{2l+1}\,\frac{1}{\bar{\rho}}\int_b^a G_l(r';\gamma,d)\,(\rho_1)_l^m(r')dr' \,,$$

where $\bar{\rho}$ is the average density of the Earth and $G_l(r';\gamma,d)$ is the dimensionless geoid kernel given in equation (B9).

References

Anderson, O.L., Schreiber, E., Lieberman, R.C. and Soga, N., 1968. Some elastic constant data on minerals relevant to geophysics, *Rev. Geophys. Space Phys.*, **6**, 491-524.

Arkani-Hamed, J., and Toksöz, M.N., 1984. Thermal evolution of venus, *Phys. Earth Planet. Int.*, **34**, 232-250.

Backus, G., 1958. A class of self-sustaining dissipative spherical dynamos, *Annals of Physics*, **4**, 372-447.

Chandrasekhar, S, 1961. *Hydrodynamic and Hydromagnetic Stability*, Oxford, University Press.

Dziewonski, A.M., 1984. Mapping the lower mantle: determination of lateral heterogeneity in P velocity up to degree and order 6, *J. Geophys. Res.*, **89**, 5929-5952.

Forte, A.M. and Peltier, W.R., 1987. Plate tectonics and aspherical earth structure: the importance of poloidal-toroidal coupling, *J. Geophys. Res.*, in press.

Hager, B.H., 1984. Subducted slabs and the geoid: constraints on mantle rheology and flow, *J. Geophys. Res.*, **89**, 6003-6015.

Hager, B.H. and O'Connell, R.J., 1978. Subduction zone dips and flow driven by the plates, *Tectonophysics*, **50**, 111-134.

Lerch, F.S., Klosko, S.M., Laubscher, C.E. and Wagner, C.A., 1979. Gravity model Improvement using GEOS 3 (GEM9 and GEM10), *J. Geophys. Res.*, **84**, 3897-3916.

Minster, J.B. and Jordan, T.H., 1978. Present-day plate motions, *J. Geophys. Res.*, **83**, 5331-5354.

Nakiboglu, S.M., 1982. Hydrostatic theory of the earth and its mechanical implications, *Phys. Earth Planet. Int.*,**28**, 302-311.

O'Connell, R.J., 1971. Pleistocene glaciation and the viscosity of the lower mantle, *Geophys. J. R. Astr. Soc.*, **23**, 299-327.

Parsons, B. and Daly, S., 1983. The relationship between surface topography, gravity anomalies, and the temperature structure of convection, *J. Geophys. Res.*,**88**, 1129-1144.

Peltier, W.R., 1982. Dyamics of the ice age earth, *Adv. Geophys.*,**24**, 1-146.

Peltier, W.R., 1985. Mantle convection and viscoelasticity, *Ann. Rev. Fluid Mech.*,**17**, 561-608.

Peltier, W.R., Drummond, R.A. and Tushingham, A.M., 1986. Post-glacial rebound and transient lower mantle rheology, *Geophys. J. R. Astr. Soc.*,**87**, 79-116.

Ricard, Y., Fleitout, L. and Froidevaux, C., 1984. Geoid heights and lithospheric stresses for a dynamic earth, *Ann. Geophys.*,**2**, 267-286.

Richards, M.A., and Hager, B.H., 1984. Geoid anomalies in a dynamic earth, *J. Geophys. Res.*,**89**, 5987-6002.

Woodhouse, J.H., and Dziewonski, A.M., 1984. Mapping the upper mantle: three-dimensional model of earth structure by inversion of seismic waveforms, *J. Geophys. Res.*,**89**, 5953-5986.

Wu, P., and Peltier, W.R., 1983. Glacial isostatic adjustment and the free air gravity anomaly as a constraint on deep mantle viscosity, *Geophys. J. R. Astr. Soc.*,**74**, 377-450.

A.M. FORTE and W.R. PELTIER, Department of Physics, University of Toronto, Toronto ON M5S 1A7, Canada.